Transient Absorption Microscopy of Monolayer and Bulk WSe_2

Qiannan Cui, Frank Ceballos, Nardeep Kumar, and Hui Zhao*

Department of Physics and Astronomy, The University of Kansas, Lawrence, Kansas 66045, United States

ABSTRACT We present an experimental investigation on the exciton dynamics of monolayer and bulk WSe_2 samples, both of which are studied by femtosecond transient absorption microscopy. Under the excitation of a 405 nm pump pulse, the differential reflection signal of a probe pulse (tuned to the A-exciton resonance) reaches a peak rapidly that indicates an ultrafast formation process of excitons. By resolving the differential reflection signal in both time and space, we directly determine the exciton lifetimes of 18 ± 1 and 160 ± 10 ps and the exciton diffusion coefficients of 15 ± 5 and 9 ± 3 cm^2/s in the monolayer and bulk samples, respectively. From these values, we deduce other parameters characterizing the exciton dynamics such as the diffusion length, the mobility, the mean free path, and the mean free length. These fundamental parameters are useful for understanding the excitons in monolayer and bulk WSe_2 and are important for applications in optoelectronics, photonics, and electronics.

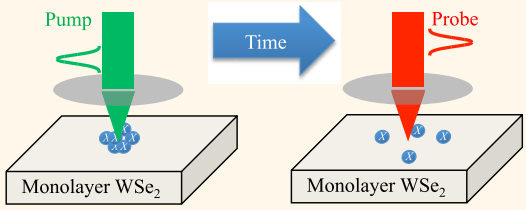

KEYWORDS: transient absorption · tungsten diselenide · exciton · 2D material · atomic layers · diffusion · transport

Tungsten diselenide is a layered semiconductor with a hexagonal crystalline structure and an indirect bandgap of 1.35 eV. Its optical properties are dominated by two direct exciton transitions at 1.71 and 2.30 eV, known as A and B excitons, respectively.[1−3] Due to its high absorption coefficients in the visible range and its resistance to photocorrosion, it has been widely used as electrodes in photoelectrochemical solar cells[4−6] and hydrogen evolution.[7] In addition, owing to its layered structure, WSe_2 is flexible and has very low surface trap density, making it an attractive candidate for flexible electronics. Previously, field effect transistors based on single crystal WSe_2 have been demonstrated, and carrier mobilities comparable to silicon at room temperature were achieved.[8−10] Furthermore, current rectification has been observed in heterojunction diodes of InAs/WSe_2.[11]

Since the discovery of graphene, significant efforts have been focused on developing two-dimensional (2D) crystals beyond graphene from other layered crystals, such as transition metal dichalcogenides.[12−15] In fact, ultrathin films containing only two layers of WSe_2 have been successfully produced by mechanical exfoliation in 1970, and the thickness effect on the exciton transitions has been revealed.[16] More recently, WSe_2 2D crystals have been fabricated by modulated elemental reaction,[17] solution-phase synthesis,[18] rapid selenization process[19] and mechanical exfoliation.[20] Photoluminescence (PL) measurements have confirmed an indirect-to-direct bandgap transition in monolayers,[21−23] which is similar to other transition metal dichalcogenides, such as MoS_2[24,25] and $MoSe_2$.[26,27] Raman spectroscopy has been used to determine the thickness and to study lattice dynamics in 2D WSe_2.[21,23,28,29] P-type field effect transistors were fabricated with monolayer WSe_2 with a high hole mobility of 250 $cm^2/(V\ s)$ and an on/off ratio of 10^6 at room temperature.[30] Later demonstration of n-type field effect transistors with comparable electron mobilities illustrated potentials of this material for complementary logic applications.[31,32] These performances are comparable to, or even better than, the more extensively studied MoS_2 monolayers.[33−35] Furthermore, first-principles calculations predicted giant spin−orbital-induced spin splittings in monolayer WSe_2 of more than 400 meV,[36] suggesting potential applications of WSe_2 2D crystals in spintronics.[37−39]

Besides being a novel material itself for various applications, as one of the only four non-carbon materials with monolayers that are known to be stable in ambient conditions,[40] WSe_2 can play important roles in

* Address correspondence to huizhao@ku.edu.

Received for review January 16, 2014 and accepted February 18, 2014.

Published online February 18, 2014
10.1021/nn500277y

developing van der Waals heterostructures and crystals.[40−48] Therefore, it is important to understand the intrinsic properties of WSe_2.

Here we report a time-resolved study of exciton dynamics in monolayer and bulk WSe_2 by transient absorption microscopy. By resolving the exciton dynamics in both time and space with high resolution, we directly measure lifetimes and diffusion coefficients of excitons in monolayer and bulk WSe_2 and deduce other parameters describing the dynamics, such as diffusion length, mean free time, mean free path, and exciton mobility. These parameters are important for understanding excitons in monolayer and bulk WSe_2 and for designing various optoelectronic devices utilizing excitons in this material.

RESULTS AND DISCUSSION

In our experiments, the excitons are injected by a 100 fs pump laser pulse and are detected by measuring the differential reflection of a probe pulse, defined as the relative change of the probe reflection due to the pump pulse. To resolve the exciton dynamics, the differential reflection is measured as a function of the probe delay, probe wavelength, and the distance between the probe and the pump laser spots. All the measurements were performed under ambient conditions with no signs of sample variation observed during the whole study. See the Method section for more details.

Figure 1a shows the differential reflection signal of the monolayer sample measured with different values of the pump pulse fluence. In these measurements, a pump pulse of 405 nm is used to excite the sample. The probe is tuned to 750 nm, close to the peak of the 1s resonance of the A-exciton. Hence, it is expected to probe the population of A-excitons. First, we analyze the data with probe delays longer than 5 ps. We find that the signal decays exponentially. By single-exponential fits with an adjustable baseline, shown as the gray curves in Figure 1a, we deduce the decay time from each curve, as plotted as the red squares in Figure 1b (left axis). In this time range, the decay of the differential reflection signal can be attributed to the loss of exciton population due to their recombination. Therefore, the decay time measures the exciton lifetime. From Figure 1b, the lifetime is independent of the pump fluence. To convert the pump fluence to the injected exciton density, we use bulk absorption coefficient of 0.5×10^6 cm^{-1}, as previous reported,[1] and assume that every pump photon absorbed excites one exciton. We find that the largest pump fluence used in these measurements (1.66 $\mu J/cm^2$) corresponds to an areal exciton density of about $1.0 \times 10^{11}/cm^2$, or an average distance between excitons of about 31 nm. In such a low density regime, it is reasonable that exciton−exciton interaction does not influence the exciton dynamics. We obtain an averaged value of

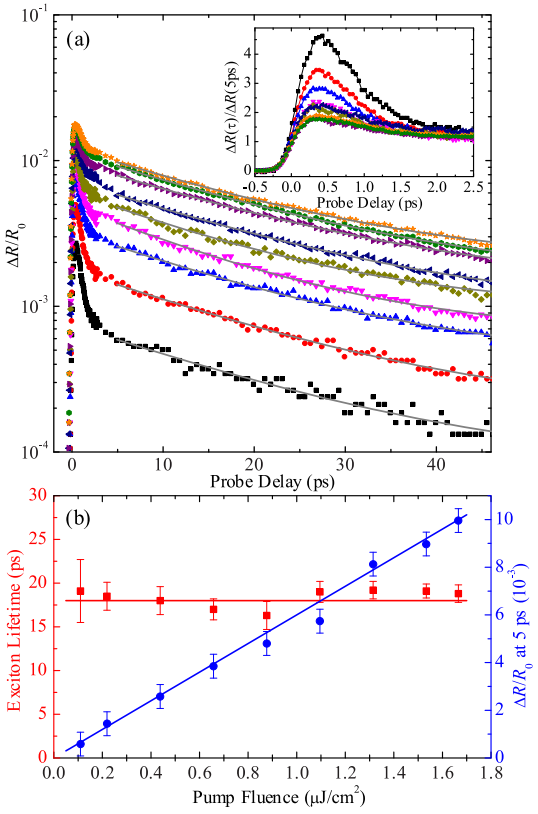

Figure 1. (a) Differential reflection of a 750 nm probe as a function of the probe delay in monolayer WSe_2 measured with a 405 nm pump of energy fluences of (from bottom to top) 0.11, 0.22, 0.44, 0.66, 0.88, 1.10, 1.31, 1.54, and 1.66 $\mu J/cm^2$. The inset shows the signal at early probe delays. (b) The exciton lifetime (red squares, left axis) and the magnitude of the signal at a probe delay of 5 ps (blue circles, right axis) as a function of the pump fluence.

the lifetime of 18 ± 1 ps, indicated as the red line in Figure 1b. The blue circles in Figure 1b show the differential reflection signal as a function of the pump fluence at a fixed probe delay of 5 ps. Clearly, the signal is proportional to the pump fluence, and hence, the injected exciton density. This further confirms the validity of using the differential reflection signal to monitor the exciton density.

Next, we focus on features observed at very early probe delays. As shown in Figure 1a, a fast component of the differential reflection is observed near the zero delay. The inset of Figure 1a provides a closer view of this time range. To better illustrate this component, each curve in the inset was divided by its value at 5 ps. Clearly, this component exist for less than 2 ps and is relatively pronounced with lower values of the pump fluence. We can rule out this component as a fast decay of exciton population. If that were the case, the differential reflection signal at 5 ps (that is, after such a process) would not be proportional to the pump fluence (injected exciton density), as shown in Figure 1b. For example, as can be seen in the inset of Figure 1a, at the lowest pump fluence used, the exciton population would have dropped by about a factor of

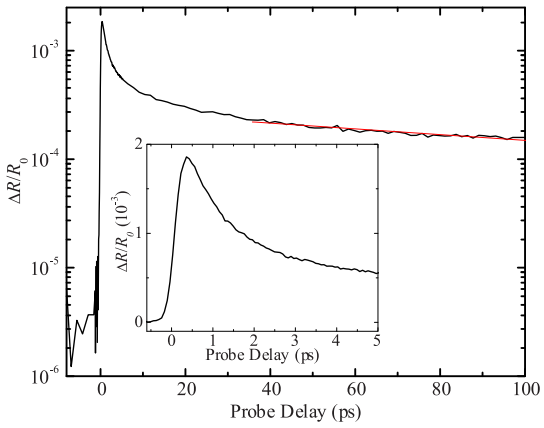

Figure 2. Differential reflection of the 750 nm probe as a function of the probe delay in bulk WSe_2 measured with a 405 nm pump fluence of 0.3 μJ/cm^2. The inset provides a closer view over the early probe delays.

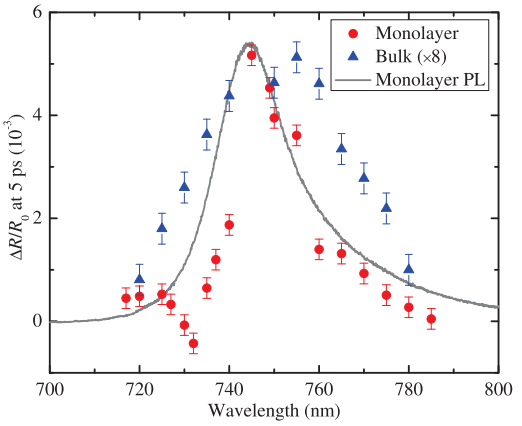

Figure 3. Differential reflection signals as a function of the probe wavelength measured in the monolayer (red circles) and bulk (blue triangles, multiplied by 8) WSe_2 samples. The 405 nm pulse has a fluence of 0.7 μJ/cm^2 and arrives 5 ps before the probe pulse. The gray line shows the PL spectrum of the monolayers sample (in arbitrary units).

5 within 2 ps, while the decrease is less than a factor of 2 at higher fluences. This would have resulted in a significant deviation from the linear relation shown in Figure 1b. We can also rule out any direct nonlinear interactions between the pump and the probe pulses, since this component persists beyond the temporal overlap of these pulses. We suspect that this component could originate from an additional contribution of the pump excitation to the differential reflection. Nevertheless, our study of the exciton dynamics after 5 ps is not influenced by this fast component, since the signal after this process is proportional to the pump fluence and the exciton density.

The 405 nm pump has a photon energy of 3.06 eV. So far, the exciton binding energies in monolayer WSe_2, as well as other transition metal dichalcogenides, have not been experimentally determined. A theory predicts a value of 0.90 eV for monolayer WSe_2.[49] Since the pump photon energy is higher the A-exciton resonance by an amount of 1.40 eV, it is safe to assume that the pump injects free carriers with a high kinetic energy, instead of excitons. By using the curves shown in the inset of Figure 1a that are measured with high pump fluences and, hence, are free of the unknown fast component, the differential reflection signal reaches a peak at about 0.3 ps. This rising time is close to the instrument response time. Such a short rising time suggests an ultrafast (subps) exciton formation process of the injected hot electron–hole pairs.

For comparison, we study a thick flake on the same substrate that is fabricated from the same crystal. Its thickness is not accurately determined; however, it is not transparent for visible light. Hence, it is at least several 10 nm thick and can be treated as a bulk sample. The experimental conditions are the same, with a pump fluence of 0.3 μ J/cm^2. The results are shown in Figure 2. We observe a similar fast rise and a fast decay [inset of Figure 2], followed by a slower decay. An exponential fit (red line) gives a decay constant of 160 $\pm$ 10 ps, which is a factor of 8 longer than monolayer. The enhanced exciton recombination in monolayer observed here is consistent with recent PL measurements that showed much higher PL yield in monolayer WSe_2 than few-layer and bulk samples.[21−23]

Previously, transient absorption measurements have been performed in monolayer MoS_2.[50−53] The spectra of the transient absorption were found to be significantly different from the absorption spectra of the samples.[50,51,53] Hence, it is interesting to measure the spectra of transient absorption in WSe_2. With a fixed 405 nm pump fluence of 0.7 μJ/cm^2, we measure the differential reflection of the monolayer flake as a function of the probe delay with various probe wavelengths. We observe the same time evolution of the signal. The red circles in Figure 3 show the magnitude of the signal at a fixed probe delay of 5 ps, together with a PL spectrum of the monolayer sample (the gray line) measured under excitation of a 632.8 nm He–Ne laser beam. We find that on the long-wavelength side of the PL peak, the differential reflection spectrum agrees very well with the PL line shape, which reflects the A-exciton resonance. However, on the short-wavelength side, there appears to be a negative component that is superimposed to the resonance. In a small wavelength range around 730 nm, the signal becomes negative. Generally speaking, the transient absorption on exciton resonances in semiconductors can be induced by several mechanisms, such as phase-space state filling,[54] screening of the Coulomb interaction,[54] and bandgap renormalization.[55] The phase-space state filling effect reduces the exciton transition strength, while the other two effects cause the exciton transition to shift and broaden. Our results indicate that on the long-wavelength side the effect is predominately

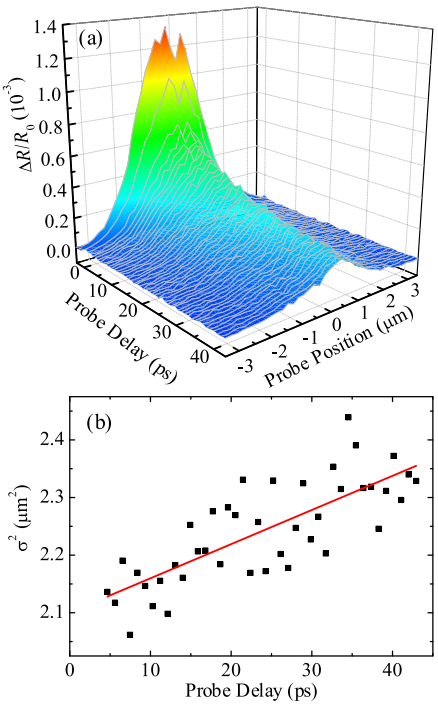

Figure 4. (a) Differential reflection signal as a function of both the probe delay and the probe position measured from the monolayer WSe_2 sample. (b) The deduced squared width of each differential reflection spatial profile as a function of the probe delay. The red line indicates a linear fit.

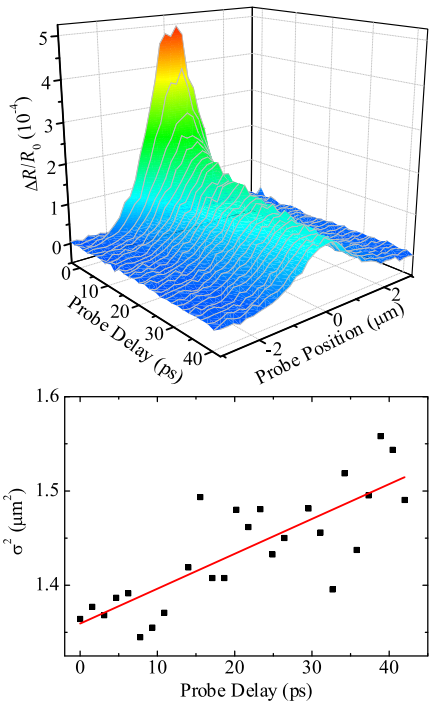

Figure 5. (a) Differential reflection signal as a function of both the probe delay and the probe position measured from the bulk WSe_2 sample. (b) The deduced squared width of each differential reflection spatial profile as a function of the probe delay. The red line indicates a linear fit.

phase-space state filling, while on the short-wavelength side, other mechanisms are also involved.

We also measure the transient absorption spectrum of the bulk sample under the same conditions. The results are shown as the blue triangles in Figure 3. Compared to the PL of monolayer, the peak is broader and is slightly shifted to longer wavelength. The negative component in the short-wavelength side is not seen.

To study the transport properties of the excitons in WSe_2, we spatially and temporally resolve the differential reflection signal.

In this measurement, the 405 nm pump and the 750 nm probe pulses are both focused to spots of about 1.3 μm (1/e intensity width) with a pump fluence of 0.7 μJ/cm^2. We adjust the distance between the centers of the pump and probe spots on the sample, and at each distance we measure the differential reflection signal as a function of the probe delay. The result of such a spatiotemporally resolved measurement is plotted in Figure 4a. To analyze the evolution of the profile, we fit the profile corresponding to each probe delay by a Gaussian function to determine its 1/e width (σ). The squared width is plotted in Figure 4b as a function of the probe delay.

The excitons injected by the tightly focused pump pulse diffuse in the monolayer WSe_2, driven by the density gradient. During this process, excitons also recombine randomly and independent of each other. Such a process can be described by the classical diffusion equation.[56] Since the initially injected profile is determined by the pump laser spot, which has a Gaussian intensity profile, the exciton density profile reminds Gaussian and broadens with time. Quantitatively, it can be readily shown that $\sigma^2(t) = \sigma_0^2 + 4Dt$, where D and σ_0 are the exciton diffusion coefficient and the initial width, respectively.[56] By a linear fit [the red line in Figure 4b], we obtain an exciton diffusion coefficient of 15 $\pm$ 5 cm^2/s.

The measurement is performed with a low-density exciton system. The peak density at the center of the profile is 2.4 $\times$ 10^{10}/cm^2, corresponding to an average distance of 63 nm between two excitons. Under this condition, the exciton transport is not influenced by the exciton−exciton interaction. It is determined by the thermal motion of excitons (at room temperature) and the exciton scattering with its environment, including phonons, lattice imperfections, and the substrate. Hence, the exciton diffusion coefficient indicates the strength of these interactions. From the measured diffusion coefficient, we deduce a mean free time (D/v_T^2, where v_T is the thermal velocity) of about 0.24 ps and a mean free path of 17 nm. Together with a lifetime of τ = 18 ps obtained in the time-resolved measurements shown in Figure 1, we obtain a diffusion length of $(D\tau)^{1/2}$ = 160 nm. These fundamental parameters on exciton dynamics are important for understanding exciton physics in monolayer WSe_2 and for its

applications in optical and photonic devices. For example, a recent study showed that PL from monolayer WSe_2 at low temperature is linearly polarized, indicating a valley coherence time that is much longer than the exciton lifetime.[38] Measurement of exciton lifetime can help estimate the valley coherence time.

For electronic applications, charge transport, instead of the exciton transport, dominates device performances. Very recently, charge transport was studied in n-type and p-type field-effect transistors made of ultrathin WSe_2.[30−32] An electron mobility of 200 $cm^2/(V\ s)$[32] and a hole mobility of 250 $cm^2/(V\ s)$[30] in monolayer WSe_2 at room temperature were deduced from these measurements. From the exciton diffusion coefficient measured here, we deduce an exciton mobility of μ = 600 $cm^2/(V\ s)$ by using the Einstein relation, $\mu = eD/k_BT$, where e, k_B, and T are elementary charge, Boltzmann constant, and temperature, respectively. Since excitons are neutral particles, their interactions with charged impurities and piezoelectric types of phonons are expected to be weaker than the charge carriers. Hence, it is reasonable that exciton mobility is slightly larger than the charge mobilities. We note that the all-optical approach used here is free of device fabrication and, hence, avoids any potential complications caused by the quality of the devices and the contacts.

For comparison, we also measure diffusion of excitons in the bulk sample under the same conditions. The results are summarized in Figure 5. We find an exciton diffusion coefficient of 9 ± 3 cm^2/s, which is comparable to the monolayer value. From this value and the lifetime of 160 ps, we deduce a diffusion length of 380 nm, a mean free time of 0.14 ps, a mean free path of 10 nm, and an exciton mobility of 350 $cm^2/(V\ s)$. Previously, electron mobilities of about 105 $cm^2/(V\ s)$[8] and hole mobilities in the range of 236−500 $cm^2/(V\ s)$[8,9] in bulk WSe_2 at room temperature have been reported. Our results are comparable to these values.

CONCLUSION

In summary, we have performed a comprehensive study of exciton dynamics in both monolayer and bulk WSe_2 samples by using femtosecond transient absorption microscopy. Excitons are generated by direct interband excitation of a 405 nm pump pulse and detected by measuring differential reflection of a probe pulse tuned near the A-exciton resonance. By spatially and temporally resolving the differential reflection signal, we directly measured the exciton lifetime and diffusion coefficient in both samples. From these values, we deduce other parameters such as diffusion length, mobility, mean free time, and mean free path. These measurements yielded fundamental parameters describing exciton dynamics in both monolayer and bulk WSe_2 that are useful for both understanding excitons in this material and applications of this material in optoelectronics, photonics, and electronics.

METHODS

The samples studied are monolayer flakes of WSe_2 fabricated by mechanical exfoliation from a bulk crystal onto a silicon substrate with a 280 nm oxide layer. Monolayer flakes are identified with an optical microscope, according to the optical contrasts enhanced by the substrate. The identified monolayer flakes are further confirmed by PL spectroscopy. Under the excitation of a 632.8 nm continuous-wave laser beam, bright PL is observed, as shown as the gray curve in Figure 3. The PL spectrum has a peak wavelength of 744 nm and a full width of about 25 nm. Both features are in good agreement with recently reported PL of monolayer WSe_2,[21−23] but significantly different from multilayer (even bilayer) flakes, which are broad and with multiple peaks.[21−23]

In the transient absorption microscopy setup, a 10 W solid state diode laser is used to pump a passively mode-locked Ti:sapphire oscillator that generates 100 fs pulses with a central wavelength of 810 nm at 80 MHz. A portion of this beam is focused to a beta barium borate (BBO) crystal to obtain 405 nm pulses by second-harmonic generation, which is used as the pump in the experiment. It is tightly focused to the sample by a microscope objective lens. The rest of the 810 nm beam is used to pump an optical parametric oscillator, which generates a signal output in the range of 1440−1580 nm. Second harmonic of this beam, generated in another BBO crystal, is used as the probe. It is focused to the sample by the same objective lens. The reflected probe is collimated by the objective lens and measured by one detector of a balanced detector. A portion of the probe beam is taken as a reference beam, which is sent to the other detector of the balanced detector. The output of the balanced detector is measured by a lock-in amplifier. A mechanical chopper is used in the pump arm to modulate the intensity of the pump beam at about 2 kHz.

The lock-in amplifier detects the differential reflection of the probe, defined as the relative change of the probe reflection by the presence of the pump, that is, $\Delta R/R_0 = (R - R_0)/R_0$, where R and R_0 are the probe reflection with and without the presence of the pump. We measure the differential reflection as a function of the time delay between the pump and probe pulses, which is controlled by moving a retroreflector installed on a linear stage. We also measure the differential reflection signal as we vary the distance between the centers of the pump and probe spots on the sample, by tilting a beamsplitter that reflects the pump beam into the objective lens. Furthermore, an imaging system based on a charge-coupled device is used to monitor the sample surface and the pump and probe spots. A spectrometer is used to measure the PL of the sample and the properties of the pump and probe pulses.

Conflict of Interest: The authors declare no competing financial interest.

Acknowledgment. We acknowledge support from the US National Science Foundation under Awards Nos. DMR-0954486 and EPS-0903806, and matching support from the State of Kansas through Kansas Technology Enterprise Corporation.

REFERENCES AND NOTES

1. Beal, A. R.; Liang, W. Y.; Hughes, H. P. Kramers-Kronig Analysis of Reflectivity Spectra of 3R-WS_2 and 2H-WSe_2. *J. Phys. C* **1976**, *9*, 2449–2457.
2. Coehoorn, R.; Haas, C.; Dijkstra, J.; Flipse, C. J. F.; Degroot, R. A.; Wold, A. Electronic-Structure of $MoSe_2$, MoS_2, and WSe_2 I. Band-Structure Calculations and Photoelectron-Spectroscopy. *Phys. Rev. B* **1987**, *35*, 6195–6202.

3. Coehoorn, R.; Haas, C.; de Groot, R. A. Electronic Structure of $MoSe_2$, MoS_2, and WSe_2. II. The Nature of the Optical Band Gaps. *Phys. Rev. B* **1987**, *35*, 6203–6206.
4. Lewerenz, H. J.; Heller, A.; Disalvo, F. J. Relationship Between Surface-Morphology and Solar Conversion Efficiency of WSe_2 Photoanodes. *J. Am. Chem. Soc.* **1980**, *102*, 1877–1880.
5. Tenne, R.; Wold, A. Passivation of Recombination Centers in N-WSe_2 Yields High-Efficiency (Greater-Than-14-Percent) Photoelectrochemical Cell. *Appl. Phys. Lett.* **1985**, *47*, 707–709.
6. Prasad, G.; Srivastava, O. N. The High-Efficiency (17.1-Percent) WSe_2 Photo-Electrochemical Solar-Cell. *J. Phys. D* **1988**, *21*, 1028–1030.
7. McKone, J. R.; Pieterick, A. P.; Gray, H. B.; Lewis, N. S. Hydrogen Evolution from Pt/Ru-Coated P-Type WSe_2 Photocathodes. *J. Am. Chem. Soc.* **2013**, *135*, 223–231.
8. Späh, R.; Elrod, U.; Lux-Steiner, M.; Bucher, E.; Wagner, S. P N Junctions in Tungsten Diselenide. *Appl. Phys. Lett.* **1983**, *43*, 79–81.
9. Podzorov, V.; Gershenson, M. E.; Kloc, C.; Zeis, R.; Bucher, E. High-Mobility Field-Effect Transistors Based on Transition Metal Dichalcogenides. *Appl. Phys. Lett.* **2004**, *84*, 3301–3303.
10. Deshpande, M. P.; Patel, J. B.; Pandya, N. N.; Parmar, M. N.; Solanki, G. K. Growth and Transport Property Measurements of Rhenium Doped Tungsten Diselenide Single Crystal. *Mater. Chem. Phys.* **2009**, *117*, 350–354.
11. Chuang, S.; Kapadia, R.; Fang, H.; Chang, T. C.; Yen, W. C.; Chueh, Y. L.; Javey, A. Near-Ideal Electrical Properties of InAs/WSe_2 Van Der Waals Heterojunction Diodes. *Appl. Phys. Lett.* **2013**, *102*, 242101.
12. Neto, A. H. C.; Novoselov, K. New Directions in Science and Technology: Two-Dimensional Crystals. *Rep. Prog. Phys.* **2011**, *74*, 082501.
13. Novoselov, K. S. Nobel Lecture: Graphene: Materials in the Flatland. *Rev. Mod. Phys.* **2011**, *83*, 837–849.
14. Wang, Q. H.; Kalantar-Zadeh, K.; Kis, A.; Coleman, J. N.; Strano, M. S. Electronics and Optoelectronics of Two-Dimensional Transition Metal Dichalcogenides. *Nat. Nanotechnol.* **2012**, *7*, 699–712.
15. Butler, S. Z.; Hollen, S. M.; Cao, L.; Cui, Y.; Gupta, J. A.; Gutiérrez, H. R.; Heinz, T. F.; Hong, S. S.; Huang, J.; Ismach, A. F.; *et al.* Progress, Challenges, and Opportunities in Two-Dimensional Materials Beyond Graphene. *ACS Nano* **2013**, *7*, 2898–2926.
16. Consador, F.; Frindt, R. F. Crystal Size Effects on Exciton Absorption Spectrum of WSe_2. *Phys. Rev. B* **1970**, *2*, 4893–4896.
17. Nguyen, N. T.; Berseth, P. A.; Lin, Q. Y.; Chiritescu, C.; Cahill, D. G.; Mavrokefalos, A.; Shi, L.; Zschack, P.; Anderson, M. D.; Anderson, I. M.; *et al.* Synthesis and Properties of Turbostratically Disordered, Ultrathin WSe_2 Films. *Chem. Mater.* **2010**, *22*, 2750–2756.
18. Antunez, P. D.; Webber, D. H.; Brutchey, R. L. Solution-Phase Synthesis of Highly Conductive Tungsten Diselenide Nanosheets. *Chem. Mater.* **2013**, *25*, 2385–2387.
19. Wang, H. T.; Kong, D. S.; Johanes, P.; Cha, J. J.; Zheng, G. Y.; Yan, K.; Liu, N. A.; Cui, Y. $MoSe_2$ and WSe_2 Nanofilms with Vertically Aligned Molecular Layers on Curved and Rough Surfaces. *Nano Lett.* **2013**, *13*, 3426–3433.
20. Li, H.; Lu, G.; Wang, Y. L.; Yin, Z. Y.; Cong, C. X.; He, Q. Y.; Wang, L.; Ding, F.; Yu, T.; Zhang, H. Mechanical Exfoliation and Characterization of Single- and Few-Layer Nanosheets of WSe_2, TaS_2, and $TaSe_2$. *Small* **2013**, *9*, 1974–1981.
21. Tonndorf, P.; Schmidt, R.; Bottger, P.; Zhang, X.; Borner, J.; Liebig, A.; Albrecht, M.; Kloc, C.; Gordan, O.; Zahn, D. R. T.; *et al.* Photoluminescence Emission and Raman Response of Monolayer MoS_2, $MoSe_2$, and WSe_2. *Opt. Express* **2013**, *21*, 4908–4916.
22. Zhao, W. J.; Ghorannevis, Z.; Chu, L. Q.; Toh, M. L.; Kloc, C.; Tan, P. H.; Eda, G. Evolution of Electronic Structure in Atomically Thin Sheets of WS_2 and WSe_2. *ACS Nano* **2013**, *7*, 791–797.
23. Zeng, H.; Liu, G.-B.; Dai, J.; Yan, Y.; Zhu, B.; He, R.; Xie, L.; Xu, S.; Chen, X.; Yao, W.; *et al.* Optical Signature of Symmetry Variations and Spin-Valley Coupling in Atomically Thin Tungsten Dichalcogenides. *Sci. Rep.* **2013**, *3*, 1608.
24. Mak, K. F.; Lee, C.; Hone, J.; Shan, J.; Heinz, T. F. Atomically Thin MoS_2: A New Direct-Gap Semiconductor. *Phys. Rev. Lett.* **2010**, *105*, 136805.
25. Splendiani, A.; Sun, L.; Zhang, Y.; Li, T.; Kim, J.; Chim, C. Y.; Galli, G.; Wang, F. Emerging Photoluminescence in Monolayer MoS_2. *Nano Lett.* **2010**, *10*, 1271–1275.
26. Tongay, S.; Zhou, J.; Ataca, C.; Lo, K.; Matthews, T. S.; Li, J. B.; Grossman, J. C.; Wu, J. Q. Thermally Driven Crossover from Indirect Toward Direct Bandgap in 2D Semiconductors: MoS_2 *versus* $MoSe_2$. *Nano Lett.* **2012**, *12*, 5576–5580.
27. Ross, J. S.; Wu, S.; Yu, H.; Ghimire, N. J.; Jones, A. M.; Aivazian, G.; Yan, J.; Mandrus, D. G.; Xiao, D.; Yao, W.; *et al.* Electrical Control of Neutral and Charged Excitons in a Monolayer Semiconductor. *Nat. Commun.* **2013**, *4*, 1474.
28. Zhao, W. J.; Ghorannevis, Z.; Amara, K. K.; Pang, J. R.; Toh, M.; Zhang, X.; Kloc, C.; Tan, P. H.; Eda, G. Lattice Dynamics in Mono- and Few-Layer Sheets of WS_2 and WSe_2. *Nanoscale* **2013**, *5*, 9677–9683.
29. Zhao, Y. Y.; Luo, X.; Li, H.; Zhang, J.; Araujo, P. T.; Gan, C. K.; Wu, J.; Zhang, H.; Quek, S. Y.; Dresselhaus, M. S.; *et al.* Inter Layer Breathing and Shear Modes in Few-Trilayer MoS_2 and WSe_2. *Nano Lett.* **2013**, *13*, 1007–1015.
30. Fang, H.; Chuang, S.; Chang, T. C.; Takei, K.; Takahashi, T.; Javey, A. High-Performance Single Layered WSe_2 P-FETs with Chemically Doped Contacts. *Nano Lett.* **2012**, *12*, 3788–3792.
31. Fang, H.; Tosun, M.; Seol, G.; Chang, T. C.; Takei, K.; Guo, J.; Javey, A. Degenerate N-Doping of Few-Layer Transition Metal Dichalcogenides by Potassium. *Nano Lett.* **2013**, *13*, 1991–1995.
32. Liu, W.; Kang, J. H.; Sarkar, D.; Khatami, Y.; Jena, D.; Banerjee, K. Role of Metal Contacts in Designing High-Performance Monolayer N-Type WSe_2 Field Effect Transistors. *Nano Lett.* **2013**, *13*, 1983–1990.
33. Radisavljevic, B.; Radenovic, A.; Brivio, J.; Giacometti, V.; Kis, A. Single-Layer MoS_2 Transistors. *Nat. Nanotechnol.* **2011**, *6*, 147–150.
34. Radisavljevic, B.; Whitwick, M. B.; Kis, A. Integrated Circuits and Logic Operations Based on Single-Layer MoS_2. *ACS Nano* **2011**, *5*, 9934–9938.
35. Late, D. J.; Liu, B.; Matte, H. S.; Dravid, V. P.; Rao, C. N. Hysteresis in Single-Layer MoS_2 Field Effect Transistors. *ACS Nano* **2012**, *6*, 5635–5641.
36. Zhu, Z. Y.; Cheng, Y. C.; Schwingenschlogl, U. Giant Spin-Orbit-Induced Spin Splitting in Two-Dimensional Transition-Metal Dichalcogenide Semiconductors. *Phys. Rev. B* **2011**, *84*, 153402.
37. Yuan, H. T.; Bahramy, M. S.; Morimoto, K.; Wu, S. F.; Nomura, K.; Yang, B. J.; Shimotani, H.; Suzuki, R.; Toh, M.; Kloc, C.; *et al.* Zeeman-Type Spin Splitting Controlled by an Electric Field. *Nat. Phys.* **2013**, *9*, 563–569.
38. Jones, A. M.; Yu, H. Y.; Ghimire, N. J.; Wu, S. F.; Aivazian, G.; Ross, J. S.; Zhao, B.; Yan, J. Q.; Mandrus, D. G.; Xiao, D.; *et al.* Optical Generation of Excitonic Valley Coherence in Monolayer WSe_2. *Nat. Nanotechnol.* **2013**, *8*, 634–638.
39. Jones, A. M.; Yu, H.; Ross, J. S.; Klement, P.; Ghimire, N. J.; Yan, J.; Mandrus, D. G.; Yao, W.; Xu, X. Spin-Layer Locking Effects in Optical Orientation of Exciton Spin in Bilayer WSe_2. *Nat. Phys.* **2014**, *10*, 130–134.
40. Geim, A. K.; Grigorieva, I. V. Van Der Waals Heterostructures. *Nature* **2013**, *499*, 419–425.
41. Gobre, V. V.; Tkatchenko, A. Scaling Laws for Van Der Waals Interactions in Nanostructured Materials. *Nat. Commun.* **2013**, *4*, 2341.
42. Haigh, S. J.; Gholinia, A.; Jalil, R.; Romani, S.; Britnell, L.; Elias, D. C.; Novoselov, K. S.; Ponomarenko, L. A.; Geim, A. K.; Gorbachev, R. Cross-Sectional Imaging of Individual Layers and Buried Interfaces of Graphene-Based Heterostructures and Superlattices. *Nat. Mater.* **2012**, *11*, 764–767.
43. Britnell, L.; Ribeiro, R. M.; Eckmann, A.; Jalil, R.; Belle, B. D.; Mishchenko, A.; Kim, Y.-J.; Gorbachev, R. V.; Georgiou, T.;

Morozov, S. V.; *et al.* Strong Light-Matter Interactions in Heterostructures of Atomically Thin Films. *Science* **2013**, *340*, 1311–1314.
44. Yu, W. J.; Liu, Y.; Zhou, H.; Yin, A.; Li, Z.; Huang, Y.; Duan, X. Highly Efficient Gate-Tunable Photocurrent Generation in Vertical Heterostructures of Layered Materials. *Nat. Nanotechnol.* **2013**, *8*, 952–958.
45. Georgiou, T.; Jalil, R.; Belle, B. D.; Britnell, L.; Gorbachev, R. V.; Morozov, S. V.; Kim, Y. J.; Gholinia, A.; Haigh, S. J.; Makarovsky, O.; *et al.* Vertical Field-Effect Transistor Based on Graphene-WS_2 Heterostructures for Flexible and Transparent Electronics. *Nat. Nanotechnol.* **2013**, *8*, 100–103.
46. Britnell, L.; Gorbachev, R. V.; Jalil, R.; Belle, B. D.; Schedin, F.; Mishchenko, A.; Georgiou, T.; Katsnelson, M. I.; Eaves, L.; Morozov, S. V.; *et al.* Field-Effect Tunneling Transistor Based on Vertical Graphene Heterostructures. *Science* **2012**, *335*, 947–950.
47. Choi, M. S.; Lee, G. H.; Yu, Y. J.; Lee, D. Y.; Lee, S. H.; Kim, P.; Hone, J.; Yoo, W. J. Controlled Charge Trapping by Molybdenum Disulphide and Graphene in Ultrathin Heterostructured Memory Devices. *Nat. Commun.* **2013**, *4*, 1624.
48. Roy, K.; Padmanabhan, M.; Goswami, S.; Sai, T. P.; Ramalingam, G.; Raghavan, S.; Ghosh, A. Graphene-MoS_2 Hybrid Structures for Multifunctional Photoresponsive Memory Devices. *Nat. Nanotechnol.* **2013**, *8*, 826–830.
49. Ramasubramaniam, A. Large Excitonic Effects in Monolayers of Molybdenum and Tungsten Dichalcogenides. *Phys. Rev. B* **2012**, *86*, 115409.
50. Shi, H.; Yan, R.; Bertolazzi, S.; Brivio, J.; Gao, B.; Kis, A.; Jena, D.; Xing, H. G.; Huang, L. Exciton Dynamics in Suspended Monolayer and Few-Layer MoS_2 2D Crystals. *ACS Nano* **2012**, *7*, 1072–1080.
51. Sim, S.; Park, J.; Song, J.-G.; In, C.; Lee, Y.-S.; Kim, H.; Choi, H. Exciton Dynamics in Atomically Thin MoS_2: Interexcitonic Interaction and Broadening Kinetics. *Phys. Rev. B* **2013**, *88*, 075434.
52. Wang, Q.; Ge, S.; Li, X.; Qiu, J.; Ji, Y.; Feng, J.; Sun, D. Valley Carrier Dynamics in Monolayer Molybdenum Disulfide from Helicity-Resolved Ultrafast Pump-Probe Spectroscopy. *ACS Nano* **2013**, *7*, 11087–11093.
53. Mai, C.; Barrette, A.; Yu, Y.; Semenov, Y. G.; Kim, K. W.; Cao, L.; Gundogdu, K. Many-Body Effects in Valleytronics: Direct Measurement of Valley Lifetimes in Single-Layer MoS_2. *Nano Lett.* **2013**, *14*, 202–206.
54. Schmitt-Rink, S.; Chemla, D. S.; Miller, D. A. B. Theory of Transient Excitonic Optical Nonlinearities in Semiconductor Quantum-Well Structures. *Phys. Rev. B* **1985**, *32*, 6601–6609.
55. Kleinman, D. A.; Miller, R. C. Band-Gap Renormalization in Semiconductor Quantum Wells Containing Carriers. *Phys. Rev. B* **1985**, *32*, 2266–2272.
56. Smith, L. M.; Wake, D. R.; Wolfe, J. P.; Levi, D.; Klein, M. V.; Klem, J.; Henderson, T.; Morkoç, H. Picosecond Imaging of Photoexcited Carriers in Quantum Wells: Anomalous Lateral Confinement at High Densities. *Phys. Rev. B* **1988**, *38*, 5788–5791.